

# Combined Electrospray-SMPS and SR-SAXS Investigation of Colloidal Silica Aggregation. Part I. Influence of Starting Material on Gel Morphology

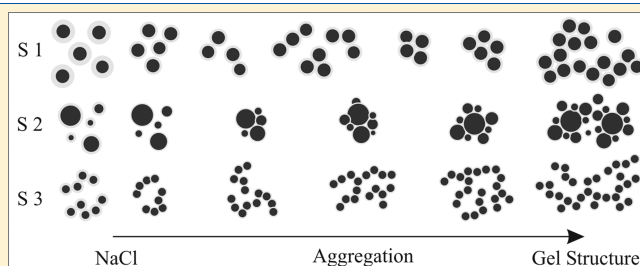
Ann-Cathrin J. H. Johnsson,<sup>\*,†</sup> M. Caterina Camerani,<sup>‡</sup> and Zareen Abbas<sup>†</sup>

<sup>†</sup>Department of Chemistry, University of Gothenburg, Kemigården 4, 412 96 Göteborg, Sweden

<sup>‡</sup>Eka Chemicals AB, a Business Unit within AkzoNobel, 445 80 Bohus, Sweden

**S** Supporting Information

**ABSTRACT:** The slow aggregation of monodisperse, polydisperse, and preaggregated silica nanoparticles was studied with an electrospray–scanning mobility particle sizer (ES-SMPS) and time-resolved synchrotron radiation–small-angle X-ray scattering (SR-SAXS). Aggregation was induced by varying the NaCl concentration to obtain a fixed gelation time of ~40 min. The combination of these techniques provides a unique tool to monitor and resolve the aggregate development in detail. The monodisperse spherical particles were converted to dimers, trimers, and eventually larger clusters as the aggregation proceeded, while the polydisperse spherical particles formed large clusters at an early stage. The initial particle shape and polydispersity had profound effects on the morphology of the aggregates; spherical primary particles produced compact spherical clusters, whereas the preaggregated dispersions formed open, elongated aggregates. All dispersions produced gels that contained free primary particles well past the point of gelation. The stability of the aggregates and the gel morphology were interpreted by relating to the structure of porous gel layers around the particles.



## 1. INTRODUCTION

Solid gels produced via the aggregation of concentrated colloidal silica dispersions are important in many applications. The silica monolith can be used as a solid state electrochemical device or as a catalyst support,<sup>1</sup> and it has recently been shown that the gelling suspension can be used as a grouting material<sup>2,3</sup> or as a soil stabilizer.<sup>4</sup> Important parameters of the solid gel such as strength and permeability depend on the overall morphology of the contiguous gel network which in turn depends on the shape, size, and stability of the aggregates formed in the initial stages of the aggregation.<sup>1,5,6</sup> The initial aggregate formation can be influenced in various ways: the shape and size distribution of the primary particles can be varied; the particles can be subjected to perikinetic or orthokinetic aggregation in the fast or slow regime;<sup>6</sup> the aggregation can be initiated by addition of electrolyte,<sup>7</sup> by addition of polymers or oppositely charged particles,<sup>8</sup> or by changing the pH.<sup>5</sup> Thus, depending on the initial conditions various solid gel structures will be obtained.

Opposite to that of other metal oxides, silica dispersions commonly exhibit a local stability maximum at the isoelectric point (pH  $\approx$  2) and a local stability minimum in the intermediate pH range.<sup>5,6</sup> Moreover, colloidal silica particles, especially in the case of smaller particles at short separation, display an additional non-DLVO repulsion.<sup>9</sup> Generally, this additional repulsion has been attributed to one of two mechanisms. According to the first mechanism water molecules hydrogen bonded to silanol surface groups form structured layers around the silica particles. In this case the additional repulsion, known as the hydration interaction, arises due

to the overlap of these structured water layers.<sup>10,11</sup> An increase in pH reduces the capacity of the surface to form hydrogen bonds because the surface silanol groups are deprotonated. Hence, the most significant contribution of the hydration interaction to the overall stability occurs in the low pH range. In the second mechanism a gel layer that consists of covalently bonded polymeric chains of silicic acid protruding from the surface,<sup>12,13</sup> and possibly even polymeric silicic acid adsorbed on the surface via hydrogen bonding,<sup>5</sup> is formed at the particle surfaces. The additional steric repulsion occurs when the gel layers overlap. An increase of the surface charge will inflate the gel layer as the charged chains within the gel layer repel each other and the chains are also repelled by the particle surface.<sup>12</sup> Thus, the steric contribution to the overall stability increases with increasing pH. In the high pH range (pH  $\approx$  9–10), it is likely that any observable non-DLVO behavior can be attributed to the steric repulsion of the gel layer at the particle surfaces.<sup>14</sup> Addition of electrolyte will cause the protruding gel layer to deflate as the charge on the chains as well as the charge of the surface is screened.<sup>12</sup>

Several techniques have been used to study the aggregation of colloidal silica including static and dynamic light scattering,<sup>9,15</sup> viscosity and turbidity measurements,<sup>16,17</sup> small-angle X-ray scattering (SAXS), small-angle neutron scattering (SANS),<sup>18,19</sup> and single particle optical sizing.<sup>20</sup> Recently, we have shown that the

**Received:** June 23, 2010

**Revised:** December 6, 2010

**Published:** January 6, 2011

combination of electrospray (ES) and a scanning mobility particle sizer (SMPS) that determines particle size can be used for kinetic evaluations of the aggregation behavior of silica dispersions.<sup>14</sup> This analysis involves a dilution of the samples, and it was shown that the dilution caused a disintegration of the 3D gel network. In light of these results it would be beneficial to simultaneously probe the unaffected gel network using a nondestructive method. For this reason we combine here the ES-SMPS method with synchrotron radiation small-angle X-ray scattering (SR-SAXS). This combination offers a number of advantages: X-rays may because of their short wavelength and good penetration be used to access the length scales relevant in describing the size of the primary particles and the aggregation of concentrated silica dispersions. More specifically, the high brilliance SR-SAXS offers the unique ability to conduct time-resolved structural in situ studies on the aggregation process and gel formation. The ES-SMPS method, in addition to particle and aggregate size distributions, provides information concerning the stability and morphology of the gel network as well as the stability of the aggregates that form the building blocks of the gel.<sup>14</sup> This combination facilitates measurement of the early steps of the aggregate formation from the very first seconds of the reaction, which have thus far not been studied in detail. To elucidate the effect of initial particle morphology and electrolyte initiator on the solid gel morphology SR-SAXS and ES-SMPS measurements were performed on three different colloidal systems. Slow perikinetic aggregation of the concentrated dispersions was initiated by addition of sodium chloride solution. A consistent model that describes the aggregation mechanisms related to the starting morphology of the particles is proposed. The effect of various electrolyte initiators on the gel morphology of these dispersions will be presented in Part II.

## 2. EXPERIMENTAL SECTION

**2.1. Materials.** Three initial particle morphologies were included in this investigation. Sol 1 contained monodisperse spherical silica particles, Sol 2 contained polydisperse spherical particles, and Sol 3 consisted of particles with a preaggregated structure. All dispersions are commercially available products that were supplied by Eka Chemicals AB and used as received. In order to access the stability of the preaggregated structure of Sol 3 two different batches with production dates 6 months apart were analyzed. Physical and chemical properties of the dispersions are listed in Table 1. From production the dispersions were stabilized with a small amount of Na<sub>2</sub>O and contained no surfactants, buffers, or additional stabilizers. Stock solutions of the electrolyte (NaCl, 10% by weight) and the buffer solution for the ES system (Ammonium acetate, 20 mM, pH 8.0) were prepared using water purified by a milli-Q purification system (18.2 MΩ cm, Synergy 185, Millipore). The sodium chloride (supra pure, Merck), ammonium acetate (pro analysi, Merck), and ammonia (pro analysi, Scharlau) were used as received.

**2.2. Size Distribution Measurements.** An ES unit (TSI Inc., ES model 3480) combined with a SMPS (TSI Inc., SMPS model 3936) were used to measure the size distribution of particles and aggregates during aggregation. This method has been described in detail elsewhere,<sup>14,21</sup> and only a short description is given here. The method is based on transfer of particles from the liquid phase to the gas phase using the ES technique, and an aerosol containing particles and aggregates from the reaction mixture is generated. The aerosol particles are subsequently selected according to size based on their electric mobility and counted. ES is widely used in mass spectrometry as a gentle ionization method yielding

**Table 1. Physical and Chemical Properties of the Investigated Colloidal Silica Dispersions<sup>a</sup>**

properties	silica dispersions			
	Sol 1	Sol 2	Sol 3 Dec	Sol 3 July
density (g cm <sup>-3</sup> )	1.3016	1.2859	1.0984	1.0977
SiO <sub>2</sub> (wt %)	40.53	39.7	14.91	14.96
pH	9.9	9.6	10.1	10.1
specific surface (m <sup>2</sup> g <sup>-1</sup> )	216	166	546	527
viscosity (cps)	16.9	4.3	8.95	6.22

<sup>a</sup> Information supplied by Eka Chemicals.

minimal molecular fragmentation in weakly bound biomolecules such as noncovalently associated protein complexes.<sup>22,23</sup> Moreover, the particles and aggregates are transferred without causing further aggregation provided that the sample has been sufficiently diluted.<sup>14</sup> It is therefore likely that the aggregates formed in the liquid phase will be transferred intact to the gas phase.

Initially, in order to determine the size of the formed aggregates, the entire size range available for the ES-SMPS setup (4–1000 nm) was analyzed. As none of the dispersions produced aggregates larger than 300 nm, a scan interval between 7 and 300 nm was used in all further experiments. Substrates for scanning electron microscopy (SEM) were prepared by impacting particles from a collimated particle beam on silicon wafers. Complete descriptions of the experimental setups are given in Johnson et al.<sup>14</sup>

**2.3. SR-SAXS Measurements.** The SR-SAXS measurements were performed at the Austrian SAXS beamline at ELETTRA (Trieste, Italy).<sup>24</sup> The beamline optics consisted of a flat double-crystal monochromator and a double-focusing toroidal mirror with a calculated photon flux at the sample of  $5 \times 10^{12} \text{ s}^{-1}$  at 8 keV. An evacuated tube was placed between the sample position and the detector to minimize scattering from air. Two different detectors were used for the experiments: a high-resolution 2D position-sensitive MAR 300 image plate scanner ( $0.095 < q < 3.29 \text{ nm}^{-1}$ ) with a readout time of the order of minutes and a smaller 2D CCD camera ( $0.075 < q < 1.75 \text{ nm}^{-1}$ ) enabling a time resolution of  $\sim 100$  ms. The sample detector distance was around 2 m for both experimental setups, and the angular range was calibrated using silver behenate as a standard. Initially, high-resolution SR-SAXS patterns from the colloidal dispersions, prior to addition of aggregation initiator, were collected at 22 °C using the MAR 300 detector. The colloidal dispersions were sealed with dental wax within quartz Lindemann capillaries (i.d. 1 mm, 20 μL) and mounted within a copper capillary holder. The exposure times were typically 300 s.

**2.4. Aggregation Experiments.** Salt-induced aggregation is usually studied by increasing the electrolyte concentration until the fast aggregation regime is reached, thereby establishing the critical coagulation concentration (CCC).<sup>7</sup> At the CCC the energy barrier preventing aggregation is negligible (less than  $K_b T$ ). As a result, the kinetics for gel formation, and most likely the formed gel structure, will be similar for a given dispersion in the presence of various counterions.<sup>14</sup> The present work was focused on the slow aggregation regime, and we aimed to create conditions where the gel evolution in the various reaction mixtures were comparable or equal. This was achieved by adjusting the bulk electrolyte concentration in the mixtures to obtain a gel time of about 40 min. The point of gelation (PoG) was determined visually as the time at which the gel surface was stationary when the beaker containing the reaction mixture was turned upside down.

**Table 2.** Electrolyte Concentrations and Wt % Silica in the Aggregation Mixtures and the Obtained Gelation Times

sample	electrolyte conc. (M)	SiO <sub>2</sub> (wt %)	gelation time (min)
ES-SMPS			
Sol 1	0.301	36.1	43
Sol 2	0.426	33.3	38
Sol 3 Dec	0.277	12.9	38
Sol 3 July	0.307	12.7	38
SR-SAXS			
Sol 1	0.313	35.9	40
Sol 2	0.426	33.3	38
Sol 3 Dec	0.277	12.9	42
Sol 3 July	0.335	12.5	37

This approach ensures that the gel formation kinetics, and most probably the gel structure, for a given dispersion are kept reasonably constant between the experiments.<sup>14</sup> The gel structures formed from dispersions with various initial morphologies are most likely not similar. However, as the gel time was kept constant, the gel networks had a similar amount of time to evolve in the various reaction mixtures. Therefore, this approach allows for comparative kinetics investigations of the aggregation of concentrated dispersions with diverse initial morphology. All silica sols (Sol 1, Sol 2, Sol 3 December, and Sol 3 July) were aggregated in the presence of NaCl at constant temperature (20 °C). To avoid local precipitation upon addition of the electrolyte solution, all experiments were performed with a solution of sufficiently low concentration and added under good agitation. When the bulk electrolyte concentrations were calculated the volume of the particles was subtracted from the total volume. Bulk electrolyte concentrations and the weight percentage SiO<sub>2</sub> in the various reaction mixtures as well as the measured gel times are listed in Table 2.

The aggregation experiments studied with the ES-SMPS system were performed in the following manner. An appropriate amount of electrolyte solution was added to the dispersion, and the reaction mixture was stirred for 20 s. Prior to mixing and throughout the aggregation sequence the temperature of the system was held constant (20 ± 0.1 °C, Lauda, RM6). At 10 min intervals samples of the mixture were analyzed with the ES-SMPS system; the sample collection continued approximately 20 min past the PoG for all reaction mixtures. To ensure that the fraction of droplets emanating from the electrospray containing more than one particle or one aggregate is negligible, the samples were diluted prior to analysis (final concentration 0.01–0.005 wt % SiO<sub>2</sub>). We are aware that the concentration in some of the samples may be lower than the solubility of colloidal silica in water.<sup>25</sup> However, we have previously shown that the rate at which the particles dissolve to monosilicic acid is low enough to not affect the measurements.<sup>14</sup>

Time-resolved SR-SAXS aggregation experiments were performed with the stopped-flow apparatus (Biologic Co., SFM-400) using a CCD detector. At the measuring point, the mixed solutions were held within quartz Lindemann capillaries (i.d. 1 mm, 20 μL). The temperature of the quartz capillary, syringes, and transfer lines of the stop-flow apparatus was held constant (20 ± 0.1 °C, Huber, Unistat CC). For our study, only 3 syringes were used: the first contained the silica dispersion, the second contained the accelerator (NaCl, ca. 10 wt %), and the third contained Milli-Q water to flush the capillary. NaOH solution could be loaded into the fourth syringe when required to clean the stop flow cell. For two reasons a

total shot volume of 50 μL was chosen: (i) this volume allowed for reproducible mixing conditions and (ii) the excess mixed solution could be collected in a beaker to visually determine the gel time for that mixture. SR-SAXS aggregation patterns were recorded with a time interval of 0.1 s. The data was corrected for spatial distortion and electronic noise and then integrated to give  $I(q)$ , the scattered intensity as a function of the scattering angle  $q$ . To follow the evolution of the gel structure past the PoG additional measurements were made. The desired proportions of the constituents were thoroughly mixed and loaded into a quartz capillary. Then the capillary was sealed and mounted within the copper sample holder. Thus, the first scattering pattern was collected at the earliest 180 s after mixing; patterns were recorded with a time interval of 10 s.

### 3. THEORETICAL ANALYSIS OF THE EXPERIMENTAL DATA

**3.1. ES-SMPS Method . Particle Electrical Mobility.** The SMPS system classifies charged particles based on their electrical mobility in air using a differential mobility analyzer (DMA). An electric field of strength  $E$  accelerates the particles toward an inner rod in the DMA, and the ease by which a particle with charge  $q$  can be moved by the electric field is known as the particle's electrical mobility,  $Z_p$ .<sup>26</sup> At a given voltage on the inner rod, particles with a given electrical mobility reach the monodisperse aerosol outlet at the bottom of the DMA. The particle diameter is related to the electric mobility and for a spherical particle in the transition regime ( $0 < Kn < 10$ )  $Z_p$  is given by<sup>27</sup>

$$Z_p = \frac{v_e}{E} = \frac{qC_c(d_p)}{3\pi\eta d_m} \quad (1)$$

where  $v_e$  is the terminal electrostatic velocity,  $C_c(d_p)$  is the Cunningham slip correction factor,  $\eta$  is the viscosity of the fluid, and  $d_m$  is the mobility diameter of the particle. For spherical particles  $d_m$  is equal to the physical diameter  $d_p$ .<sup>28</sup> The slip correction factor depends on the diameter of the particle and is given by<sup>26</sup>

$$C_c(d_p) = 1 + Kn \left[ \alpha + \beta \exp\left(\frac{-\gamma}{Kn}\right) \right] \quad (2a)$$

$$Kn = \frac{2\lambda}{d_p} \quad (2b)$$

where  $\lambda$  is the mean free path of the gas. Allen and Raabe determined the values of the constants  $\alpha$ ,  $\beta$ , and  $\gamma$  for spherical solid particles at standard conditions.<sup>29</sup>

For nonspherical particles the particle electrical mobility can be related to the volume equivalent diameter of the particle,<sup>26</sup> i.e., the diameter of a sphere with a volume equal to the volume of the nonspherical particle. Hence,  $Z_p$  is given by<sup>28</sup>

$$Z_p = \frac{qC_c(d_m)}{3\pi\eta d_m} = \frac{qC_c(d_{ve})}{3\pi\eta d_{ve}\chi_t(\theta)} \quad (3)$$

where  $d_{ve}$  is the volume equivalent diameter and  $\chi_t(\theta)$  is the orientation-dependent dynamic shape factor of the nonspherical particle in the transition regime. Rearrangement of eq 3 gives the following relationship between the measured  $d_m$  and the volume equivalent diameter of the nonspherical particle

$$d_m = d_{ve}\chi_t(\theta)\frac{C_c(d_m)}{C_c(d_{ve})} \quad (4)$$



For particle Reynolds numbers well below 0.1 the particle orientation is random,<sup>27</sup> and orientation-averaged dynamic shape factors for particles of different shapes and aspect ratios have been reported.<sup>26</sup> In the present investigation the nonspherical particles were modeled as prolate ellipsoids with a volume given by

$$V = \frac{4\pi ab^2}{3} \quad (5)$$

where  $a$  and  $b$  correspond to the polar and equatorial radii, respectively; the aspect ratio is given by  $a/b$ .

**Fitting of Size Distributions.** All size distributions obtained from the ES-SMPS measurements were normalized according to the procedure described by Johnson et al.<sup>14</sup> A Gaussian or Log–Gaussian distribution was fitted to the size distributions obtained for the pure dispersions. The polydispersity,  $p$ , of a distribution is given by

$$p = \sqrt{\frac{\overline{r^2} - \bar{r}^2}{\bar{r}^2}} = \sqrt{\frac{\sigma_r^2}{\bar{r}^2}} \quad (6)$$

where  $\bar{r}$  is the mean and  $\sigma_r^2$  is the variance of the distribution. This gives for the Gaussian distributions a polydispersity,  $p_G$ , of

$$p_G = \frac{\sigma_r}{\bar{r}_m} \quad (7)$$

and for the Log–Gaussian distributions a polydispersity,  $p_{L-G}$ , of

$$p_{L-G} = \sqrt{e^{w^2} - 1} \quad (8)$$

where  $w$  is the width of the distribution.

Once the dispersions started to aggregate bimodal size distributions were obtained. To account for the formation of aggregates the distribution fitted to a specific pure dispersion was combined with a second Gaussian distribution. The mean diameter of the aggregates was taken as the fitted mean diameter of the second distribution, and the polydispersity of the aggregates was determined from the fit.

**3.2. Fitting of SR-SAXS Data.** The SR-SAXS data were analyzed, after radial integration of the two-dimensional patterns, by fitting to model expressions for the form and structure factors using the program FISH.<sup>30</sup> Prior to data analysis the scattering curves were normalized to the incident intensity of the beam and air scattering. Also, the scattering from a Lindemann tube filled with water was subtracted from the data, and the scattered intensity was corrected to absolute intensities. A brief description of the interpretation of small angle scattering patterns is given below; for a more detailed description see, for instance, refs 31–33.

The absolute scattering intensity,  $I(q)$ , for homogeneous hard spheres can be written as

$$I(q) = N_p V_p^2 (\Delta\delta)^2 P(q) S(q) \quad (9)$$

where  $N_p$  is the concentration of scattering particles,  $V_p$  is the volume of one scattering particle,  $\Delta\delta$  is the scattering contrast (for SR-SAXS this is the electron density difference between the silica particle and the solvent),  $P(q)$  is the single-particle form factor describing the angular distribution of the scattering due to the size and shape of the particle, and  $S(q)$  is the structure factor.  $S(q)$  accounts for any interparticle interference arising from particle spatial correlations in concentrated systems; in the dilute case,  $S(q) \approx 1$ . For anisotropic or polydisperse dispersions  $I(q)$

cannot be written as product of the form and structure factors; the exact expressions can be found in the literature.<sup>34</sup>

Analytical expressions for  $P(q)$  are known for shapes such as spheres, rods, cylinders, ellipses, etc.  $P(q)$  for monodisperse spheres is given by

$$P(q) = \left[ \frac{3(\sin(qr) - qr \cos(qr))}{(qr)^3} \right]^2 \quad (10)$$

where  $r$  is the radius of the particle.<sup>34</sup> For homogeneous ellipsoids with polar radius  $a$  and equatorial radius  $b$ , the orientation-averaged form factor is given by

$$P(q) = \int_0^1 \left| \frac{3j_1(v)}{v} \right|^2 d\mu \quad (11)$$

where

$$v = Q[a^2\mu^2 + b^2(1-\mu^2)]^{1/2} \quad (12)$$

and  $j_1$  is the first-order spherical Bessel function.<sup>31</sup>

Given that some of the colloidal dispersions included in this study are highly concentrated ( $\sim 40$  wt % SiO<sub>2</sub>), it was necessary to account for the  $S(q)$  scattering contribution. It has been shown that the hard-sphere structure factor successfully describes the interactions in these dispersions.<sup>35,36</sup> Further, this structure factor works well for soft particles and clusters of soft particles.<sup>37,38</sup> For these reasons the hard-sphere model<sup>39</sup> modified to allow for polydispersity or nonspherical shapes of the particles was chosen to describe the interactions in the reaction mixtures. For the spherical particles the Schultz distribution function was used and the polydispersity of this distribution is given by<sup>40</sup>

$$p_s = \frac{1}{(Z+1)^{1/2}} \quad (13)$$

where  $Z$  is a width parameter. This distribution can attain a Gaussian or a Log–Gaussian depending on the value of  $Z$ <sup>30</sup> and can thus be used to describe both the pure dispersions and the reaction mixtures.  $S(q)$  for nonspherical particles was corrected by an effective sphere diameter,  $d$ , obtained using an equivalent volume approximation

$$V = \frac{4}{3}\pi \left(\frac{d}{2}\right)^3 \quad (14)$$

where for an unaggregated system  $V$  is the volume of a single scattering particle. The polydispersity of the nonspherical particles could unfortunately not be assessed as it was not included in the FISH program.<sup>30</sup>

## 4. RESULTS

**4.1. Characterization of Initial Particle Morphology.** The normalized size distributions of the starting materials Sol 1, Sol 2, and Sol 3, as obtained by ES-SMPS, are shown in Figure 1. Sol 1 displayed a Gaussian distribution, while Sols 2 and 3 could be fitted to a Log–Gaussian. The mean diameters and polydispersities obtained by the fits are listed in Table 3. SEM images of the pure dispersions are shown in Figure 2. The mean diameters of Sols 1 and 2, as measured from the images, were approximately 27 and 30 nm, respectively (Figure 2a and 2b). The SEM images of Sol 3 showed that the dispersion contained preaggregates consisting of spherical primary particles with a diameter of

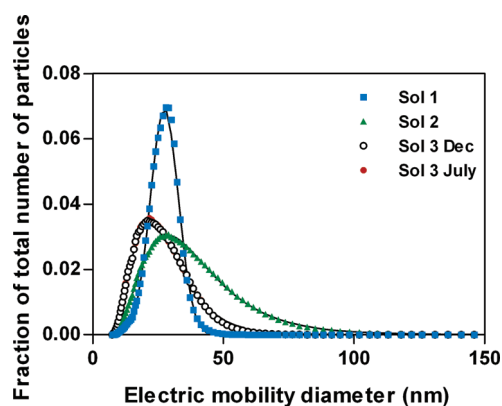


**Figure 1.** Size distributions of the pure silica dispersions; fitted distributions are shown as solid lines. The fraction plotted on the ordinate axis represents the number of particles in a size interval divided by the total number of particles in all size intervals.

**Table 3.** Fitted Distributions and Models Used Together with the Mean Diameters and the Polydispersities Obtained with ES-SMPS and SR-SAXS Methods for the Pure Dispersions

sample	ES-SMPS		
	fitted distribution	mobility diameter (nm)	polydispersities
Sol 1	G <sup>a</sup>	27.4	0.20
Sol 2	L-G <sup>b</sup>	28.5	0.50
Sol 3 Dec	L-G	21.9	0.43
Sol 3 July	L-G	21.8	0.42

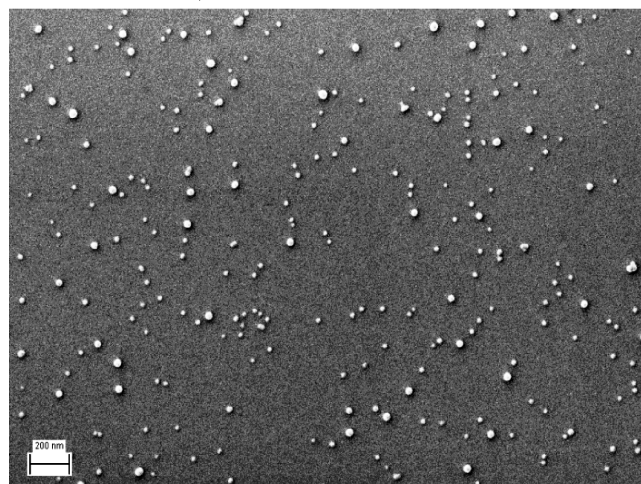
sample	SR-SAXS		
	model	D1/D2 (nm)	Hard Diameter (nm) polydispersities
Sol 1	HS <sup>c</sup>	15.8	24.8 0.13
Sol 2	HS	22.4	26.6 0.43
Sol 3 Dec	EHS <sup>d</sup>	5.8/22.4	14 n/a
Sol 3 July	EHS	6.4/22.4	14.6 n/a

<sup>a</sup> Gaussian. <sup>b</sup> Log-Gaussian. <sup>c</sup> Hard sphere. <sup>d</sup> Ellipsoidal hard sphere.

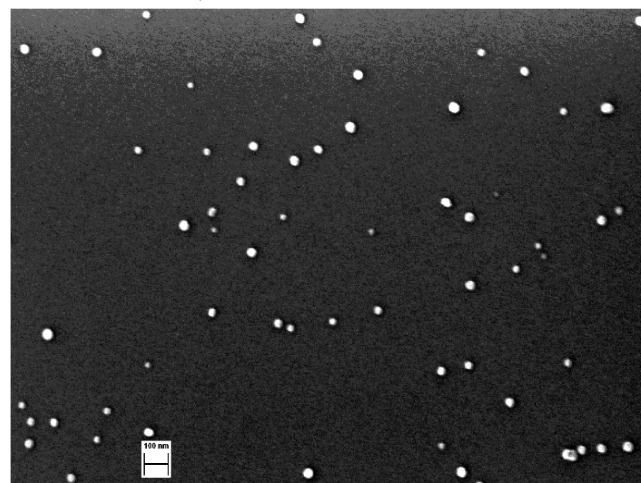
10–15 nm (Figure 2c). The preaggregates displayed a range of nonspherical shapes from straight chains to more compact clusters, and a few aggregates demonstrated a more branched structure. A majority of the preaggregates could be classified as spheres, chains, or compact clusters, and the volume of these structures can be approximated as ellipsoids. Therefore, the volume of the preaggregates was modeled as prolate ellipsoids, and average equatorial and polar diameters of 16 and 38 nm, respectively, were obtained from the images, which corresponds to an average aspect ratio of 2.3. These are arithmetic averages, and it should be noted that the preaggregates were quite polydisperse. Some of the elongated preaggregates showed polar diameters as long as 70–90 nm.

Figure 3 shows the scattered intensity as a function of the scattering vector  $q$  for the initial silica dispersions. For Sols 1 and 2 the data were fitted to the analytical expressions for the scattering arising from a spherical form factor with a hard-sphere interaction and a flat background. The scattering curves of the preaggregated samples (Sol 3 Dec and Sol 3 July) were fitted to the mathematical expression for the scattering of ellipsoidal particles with hard-sphere interactions; all fits are shown as solid lines

a) Sol 1, scale bar 200 nm.



b) Sol 2, scale bar 100 nm.



c) Sol 3, scale bar 200 nm.

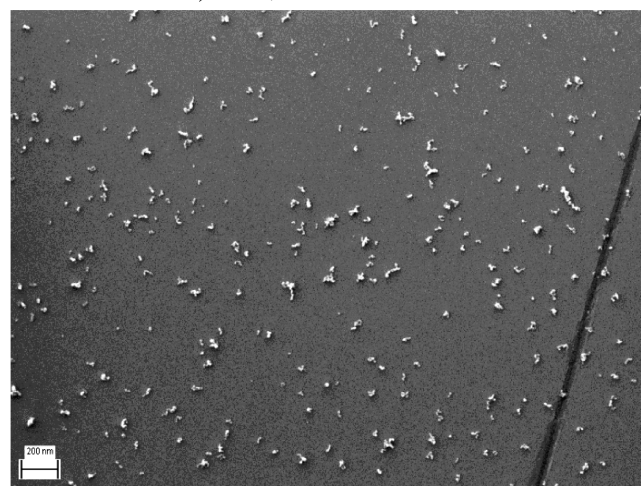


**Figure 2.** SEM images of the pure silica dispersions.

in Figure 3. The mean diameters and polydispersities obtained from the SR-SAXS analysis of the pure dispersions are listed in Table 3. Two parameters, i.e., the particle diameter (D1) and the hard-sphere diameter (HD), were obtained from the fitting of the hard-sphere model to the SR-SAXS data. When the ellipsoidal



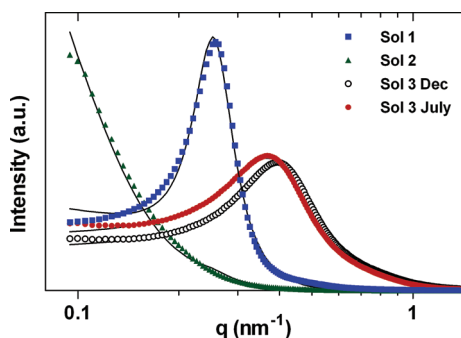


**Figure 3.**  $I(q)$  vs  $q$  for the pure silica dispersions; fits to the models are shown as solid lines.

hard-sphere model (EHS) was used three particle diameters (D1, D2, and HD) were obtained. The HD represents the closest distance of approach between two particles in the dispersion. It incorporates the electrostatic interaction of particles, the electrostatic contribution from gel layer surrounding the silica particles, and any possible hydration of the surface, while the D1s values and in the case of ellipsoidal particles D1s and D2s represent the dimensions of the scattering entity.

In the case of Sol 1 the  $I(q)$  curve showed a maximum in intensity at  $q = 0.257 \text{ nm}^{-1}$ ; thus, the curve is dominated by the structure factor contribution that arises from the interparticle interactions. A weak second order of the correlation length of the main  $S(q)$  peak was also observed as a small hump in the  $I(q)$  curve at approximately  $q = 0.5 \text{ nm}^{-1}$ ; it can be related to the packing of the primary particles in the solution. For Sol 2 no strong structure factor peak was observed, and the sample showed a significantly higher polydispersity as compared to Sol 1 (Table 3). The effects of polydispersity are not included in the ellipsoidal form factor, and the polydispersities of the two batches of Sol 3 could, therefore, not be assessed.<sup>30</sup> The aging of Sol 3 resulted in an increase of the mean equatorial diameter, while the mean polar diameter remained constant (Table 3).

**4.2. Silica Aggregation.** The size distribution variation during the aggregation of Sol 1, as obtained by ES-SMPS, is shown in Figure 4. All size distributions were normalized according to the procedure described in Johnson et al.<sup>14</sup> Bimodal size distributions were obtained for the aggregating samples, and a sum of two Gaussian distributions was fitted to the normalized size distributions (Figure 4). Past the PoG only the agglomerates, aggregates, and primary particles detachable from the three-dimensional (3D) gel network are visible using the ES-SMPS method.<sup>14</sup> In this context detachable refers to the ability of the particles and aggregates to separate from the gel structure. The obtained bimodal size distributions indicate that free primary particles were still present in the gel and both aggregates and primary particles were detachable from the gel structure well past the PoG. The other dispersions also showed primary particles present in all samples, and the sums used to fit all bimodal distributions are listed in Table 4.

The aggregate mean diameters obtained in the fitting procedures were used to calculate the mean aggregate volumes; the aggregate volumes were then normalized to the electrolyte and  $\text{SiO}_2$  concentrations in the reaction mixtures. The electrolyte and  $\text{SiO}_2$  concentrations in the four reaction mixtures that were analyzed are listed in Table 2. Initial aggregation rates, taken as the slope of the normalized aggregate volume increase, are listed in Table 4. For all dispersions analyzed the total aerosol particle mass decreased drastically at the PoG. This indicates a decrease

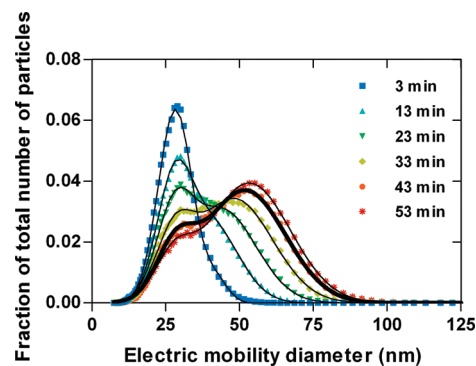


**Figure 4.** Size distribution variation during NaCl-induced aggregation of Sol 1. Fitted distributions are shown as solid lines; bold line corresponds to the distribution fitted to the point of gelation sample.

**Table 4.** Fitted Distributions and Models Used for the Aggregation Mixtures, and Initial Aggregation Rate As Obtained by ES-SMPS

sample	ES-SMPS fitted sum	SR-SAXS model	initial rate $\times 10^{-25} (\text{m}^3 \text{s}^{-1})$
Sol 1	$G^a + G$	$\text{HS}^c$ or $\text{EHS}^d$	1.95
Sol 2	$L-G^b + G$	HS	2.61
Sol 3 Dec	$L-G + G$	EHS	4.90
Sol 3 July	$L-G + G$	EHS	4.30

<sup>a</sup> Gaussian. <sup>b</sup> Log-Gaussian. <sup>c</sup> Hard sphere. <sup>d</sup> Ellipsoidal hard sphere.

in the amount of detachable particles and aggregates in the size range assessable to the ES-SMPS instrument (7–1000 nm). The drop off in aerosol mass increased in the following order: Sol 1 < Sol 2 < Sol 3 Dec  $\approx$  Sol 3 July.

The analyzed size range (7–300 nm) was divided in four size intervals (7–30, 30–40, 40–50, and 50–300 nm), and the fraction of the total number of particles (FTP) in these size intervals was calculated. The size intervals were chosen as such because Sol 1, which was used as a point of reference owing to the simple morphology of this dispersion, showed a clear sequential increase in these specific size intervals. Figure 5 illustrates the variation of the FTP during aggregation. Initially, Sol 1 (Figure 5a) showed an increase in the size range 30–40 nm; this increase peaked around 500 s simultaneously as the 40–50 nm range started to increase. At about 1000 s the range 50–300 nm began to increase linearly. As can be seen a substantial amount (almost 25%) of the total number of particles (TP) detached from the Sol 1 gel samples were unaggregated primary particles. For Sol 2 the 50–300 nm range started to increase linearly immediately after electrolyte addition while the FTP in the size intervals 30–40 and 40–50 nm remained almost constant throughout the aggregation process. The gels of Sol 2 also contained detachable primary particles and aggregates, and almost 20% of the TP detached from the gel were in the size interval 7–30 nm (Figure 5b). During the aggregation of Sol 3 only a small increase of the FTP in the size ranges 40–50 and 50–300 nm was seen. At the PoG the FTP in the size interval 7–30 nm started to increase while the FTP in the other intervals started to decrease (Figure 5c and 5d). The detachment of aggregates from the 3D gel structure of these gels was almost negligible.

The sequence of  $I(q)$  vs  $q$  plots for the aggregation of Sol 1, as followed in the stop-flow cell with the CCD detector, is shown in

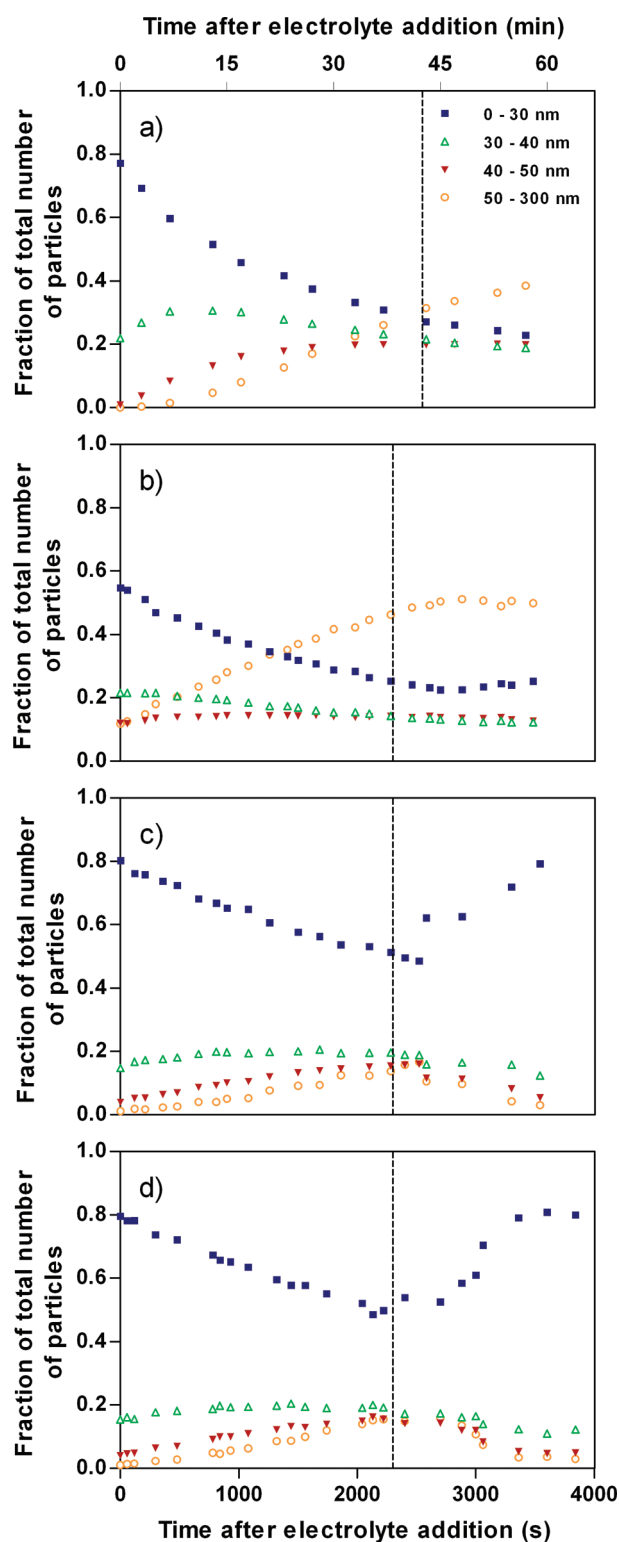


Figure 5. Change in the fraction of total number of particles: (a) Sol 1, (b) Sol 2, (c) Sol 3 Dec, and (d) Sol 3 July. The dashed vertical lines correspond to the point of gelation.

Figure 6. Each curve is shifted vertically, and only every fifth curve (every 50 s) is plotted for clarity. The initial curve for Sol 1, acquired before addition of salt, overlays the data taken in the static capillary with the MAR detector. The bold curve corresponds to the PoG, and the measurements continued  $\sim 5$  min

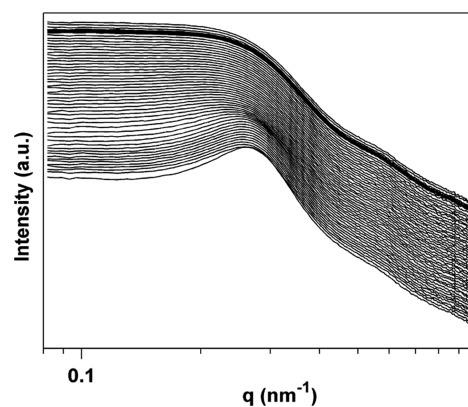


Figure 6.  $I(q)$  vs  $q$  for the NaCl-induced aggregation of Sol 1.

Table 5. Changes in Aggregate Mean Diameters and Polydispersities during the Aggregation Process

sample	ES-SMPS		SR-SAXS		
	mobility diameter (nm)	polydispersity part./agg.	D1/D2 (nm)	hard diameter (nm)	polydispersity
Sol 1 <sub>initial</sub>	27.9	0.20/0.26	15.3	23.6	0.16
Sol 1 <sub>500 s</sub>	35.9	0.19/0.26	15.4/31.3	23.6	n/a
Sol 1 <sub>1500 s</sub>	45.1	0.21/0.27	15.3/38.3	23.4	n/a
Sol 1 <sub>gel point</sub>	51.8	0.23/0.27	50.2	23.8	0.19
Sol 1 <sub>final</sub>	54.7	0.23/0.26	50.4	23.8	0.19
Sol 2 <sub>initial</sub>	28.4	0.49/0.27	20.6	27	0.39
Sol 2 <sub>500 s</sub>	56.9	0.53/0.27	54.3	29.2	0.25
Sol 2 <sub>final</sub>	68	0.76/0.28	62.8	30.4	0.20
Sol 3 Dec <sub>initial</sub>	21.5	0.43/0.23	5.4/66.4	8.2	n/a
Sol 3 Dec <sub>gel point</sub>	46.1	0.41/0.29	5.4/91.2	13.2	n/a
Sol 3 Dec <sub>final</sub>	38.5	0.41/0.31	5.4/108	17.6	n/a
Sol 3 July <sub>initial</sub>	20.4	0.41/0.26	5.6/40.0	8.4	n/a
Sol 3 July <sub>gel point</sub>	47.1	0.43/0.29	5.6/86.8	10.5	n/a
Sol 3 July <sub>final</sub>	36.2	0.40/0.31	5.6/93.5	13.2	n/a

past the PoG. A change in the scattering pattern was observed as the aggregation progressed. The peak related to interparticle interference effects shifted toward lower  $q$ , from about 500 to 1000 s after mixing, indicating an increased interparticle distance. The structure peak was obscured by the increasing intensity at lower  $q$  ( $q < 0.2 \text{ nm}^{-1}$ ) at about 1500 s after mixing. Very little further evolution of the structure was observed within the curves, even after the PoG (Figure 6). During the course of the aggregation there was almost no change in the shape or intensity of the curve at higher  $q$  ( $q > 0.4 \text{ nm}^{-1}$ ). In contrast to Sol 1, only a small variation in the low  $q$  region was seen during the aggregation of Sols 2 and 3. Possibly the polydispersity of these products masked the aggregate formation. The SR-SAXS models used to fit the scattering curves of the dispersions are listed in Table 4.

The diameters obtained from the fitting of the SR-SAXS and ES-SMPS data sets acquired for Sol 1 directly after NaCl addition, at 500 s, at 1500 s, at the PoG, and for the final sample collected are presented in Table 5. For Sol 2, Sol 3 Dec, and Sol 3 July only the diameters obtained for selected points are shown. Table 5 extended in the Supporting Information contains the

diameters obtained at all five points for all the investigated dispersions. Upon addition of the accelerator the hard diameters (HDs) of the primary particles in Sols 1 and 3 were reduced, while the HD of Sol 2 started to increase immediately after addition (compare the SR-SAXS data in Tables 3 and 5). No considerable change in aggregate size after gelation was observed in the case of Sol 1, while Sols 2 and 3 showed a more dynamic structure that evolved after the PoG. The agglomerates formed from Sol 3 grew mainly in the direction of the polar axis, and the growth was more pronounced in the newer sample (Sol 3 Dec). Generally, the aggregates formed in the newer batch of Sol 3 were larger than in the older one. Also, for Sol 2 a clear decrease in the polydispersity during agglomeration was observed.

## 5. DISCUSSION

**5.1. Initial Particle Morphology.** The SR-SAXS data analysis and SEM images confirmed that the particles in Sols 1 and 2 were spherical, and the mobility diameters ( $d_m$ 's) obtained with ES-SMPS for Sols 1 and 2 correlated well with the diameters determined from the SEM images. Evaporation of the droplets formed by electrospray results in solid silica particles and aggregates with a small amount of evaporation residues. Depending on the particle properties a complete dehydration may be hard to achieve,<sup>41</sup> and residual water may keep the gel layer inflated during the ES-SMPS analysis. Thus, both the  $d_m$ 's and SEM diameters include at least a partially inflated gel layer, and it is possible that the layer remains fully inflated. The HDs reflect the total particle–particle interaction in the dispersion, and the fact that the obtained HDs are so close to the  $d_m$ 's and SEM diameters suggests that the gel layer contributed substantially to the total interaction. In other words, the electrostatic interaction in the pure dispersions was weak. The gel layer is likely to have different scattering properties compared to the bulk of the particle. The scattering properties may also change within the gel layer, i.e., the gel close to the core particle may be similar to that of the particle bulk, while the gel close to the solvent may scatter in a manner more similar to the solvent. Evidently the gel layer, while visible in the SEM images and detectable with the ES-SMPS method, was not detected as a part of the scattering entities. Therefore, we propose that the diameters listed as D1 and D2 in Tables 3 and 5 correspond to the diameter of the particle core and that the HDs represent the diameter of the entire particle. Due to evaporation residues a small increase in the size of the particles may occur; this might be the reason why the  $d_m$ 's were 1–2 nm larger compared to the HDs.

The polydispersities of Sols 1 and 2 were assessed using both SR-SAXS and ES-SMPS. The electrospray method resulted in a higher polydispersity for both dispersions (Table 3). This is mainly due to the fact that the SR-SAXS measurements give information concerning the polydispersity of D1, which is connected to the core particles, while the ES polydispersity should include the particle gel layer as well. It is likely that the core particles have a more narrow size distribution and that the build-up of the gel layer on the particle surface will broaden the distribution. Furthermore, the diffusion of smaller particles within the differential mobility analyzer during the particle classification will also result in a broader distribution.<sup>14</sup>

The scattering curves of Sol 3 fitted well to the EHS model, suggesting an elongation of the scattering objects (Table 3). A broad maximum, related to interparticle interference, could be seen in the  $I(q)$  curve at  $q = 0.394 \text{ nm}^{-1}$  (Figure 3). Both the SR-SAXS measurements and the SEM images indicated that the

preaggregates consisted of on average four to five spherical primary particles. The preferred end-to-end addition of the primary particles is possibly due to the charge distribution on the surface of the forming preaggregates.<sup>42</sup> The HDs of Sol 3 corresponded well to the mean equatorial diameter of the preaggregates, as measured from SEM images. These results indicate that the HD values measured for Sol 3 corresponded to the full diameter of the primary particles in the preaggregates. As previously described, the HD is considered as a full particle diameter that includes the particle gel layer. Therefore, the difference between core particle diameter (D1) and the HD can be regarded as the extension of the gel layer. The polar diameters, listed as D2 in Table 3, do not include the gel layer of the primary particles. If the extension of the gel layer on both sides of the ellipse is included the polar diameter of the average aggregate is approximately 31 nm.

The mobility diameters obtained by ES-SMPS measurements of the nonspherical particles are related to the volume equivalent diameter of the particles, see eq 4. The volume equivalent diameter of an ellipsoid with an equatorial diameter of 14 nm and a polar diameter of 31 nm is  $\sim 20$  nm (eq 5). As measured from SEM images, the equatorial and polar diameters were 16 and 38 nm, respectively, which gives a calculated  $d_{ve}$  of 21.3 nm. The  $d_m$  measured for a specific nonspherical particle should be larger than the  $d_{ve}$  of the particle (eq 4).<sup>28</sup> The correct  $d_{ve}$  values are obtained by compensating the obtained  $d_m$  for the drag of the nonspherical particle. Most often the  $d_{ve}$  values are unknown a priori, but in this study these could be obtained separately from the SEM images. It was found that the uncorrected  $d_m$ , listed in Table 3, were approximately equal to the  $d_{ve}$  calculated from SEM data. Therefore, we conclude that in these measurements it was not necessary to perform the corrections stated in eq 4. Possibly the slip correction ratio cancels the dynamic shape factor contribution in this size range so that the  $d_{ve}$  is approximately equal to the measured  $d_m$ .

To assess the effect of aging on the preaggregated structures a second batch of Sol 3, Sol 3 July being 6 months older than Sol 3 Dec, was included in the investigation. With aging D1 and HD increased while D2 and  $d_m$  remained constant (Table 3). These results suggest that the preaggregated structure of the Sol 3 dispersion was stable as no addition of free particles to the aggregates or joining of preaggregates was observed. The increase in the shorter dimension is attributed to Ostwald ripening.<sup>5,43</sup> The radius of curvature at the point of primary particle contact was negative and extremely small. This leads to a low solubility of silica in this region; thus, the dissolved silica will primarily be deposited around the point of contact. No significant effect of aging was observed using the ES method because the observed morphological changes of the preaggregates results in an insignificant change of the  $d_{ve}$  and, hence, only a minor change in the  $d_m$  (Table 3). Even though the hard diameter increased, suggesting an increase in the extension of the gel layer, the innermost parts appear to consolidate and thus transforming this part of the gel layer into the denser particle core.

**5.2. Gel Formation . Effect of Electrolyte Addition.** When an electrolyte solution is added to a silica dispersion two distinct effects that destabilize the dispersion will occur simultaneously. First, the long-range interparticle electrostatic repulsion is decreased as a result of the surface charge screening.<sup>7</sup> Second, the gel layer extension decreases when the charges in the gel layer are screened; thus, the short-range steric repulsion caused by the gel layer overlap decreases.<sup>12</sup> This combined effect of electrolyte addition is apparent when the HDs obtained for the pure sols



(Table 3) are compared with the HDs obtained for the sols just after electrolyte addition (Table 5, initial). Given that the gel layer was found to contribute significantly to the hard diameter, the observed decrease of the HDs is mainly attributed to a decrease in the extension of the gel layer. The gel layer contraction increased accordingly Sol 1 < Sol 3 Dec < Sol 3 July. For Sol 2, however, the hard diameter started to increase immediately after addition. A high cross-linking within the gel layer should result in an inflexible layer that display a small contraction upon electrolyte addition, such as Sol 1. The large contraction of the Sol 3 gel layers suggests that these layers had a low cross-linking; a more flexible layer will contain a larger number of free silanol groups. Hence, it is likely that these surfaces are more reactive.

For all dispersions analyzed a decrease in D1 as a result of salt addition could also be observed. This indicates that the gel layers were fully penetrable with respect to the counterions and that addition contracted the core particles as well. The contraction of the core particles increased in the following order: Sol 3 Dec < Sol 1 < Sol 3 July < Sol 2. The large D1 decrease for Sol 2 is especially interesting as that dispersion simultaneously showed an increase in the HD. Since the Sol 2 gel layer initially was thin and the particle core diameter decreased indicating that the ions penetrated the layer, it is most likely that these gel layers were completely collapsed upon addition of the electrolyte. One explanation for the immediate increase of the HD could be that smaller particles rapidly attached to one large particle, causing the distance of closest approach to increase. This type of aggregation behavior is further supported by the rapid increase of aggregates in the 50–300 nm size range immediately after electrolyte addition *vide infra*.

*Influence of Spherical Primary-Particle Shape.* It is evident that the Sol 1 aggregation starts with the formation of dimers; the FTP in the size range 30–40 nm, which corresponds to the calculated  $d_{ve}$  for a dimer consisting of two mean Sol 1 particles (34.5 nm), showed an initial increase upon electrolyte addition (Figure 5a). The relative concentration of dimers peaked at 500 s and started to decrease as the aggregation proceeded. The formation of dimers, which should have appeared as an increase in the scattering intensity at lower  $q$ , was not immediately apparent in the scattering pattern during the first 500 s (Figure 6). However, when fitted to the EHS model the scattering pattern indicated that the majority of the aggregates in the mixture were dimers. We suggest that the early increase in the scatter intensity at low  $q$  was masked by the structural peak. Approximately 30% of the TP were dimers according to the ES-SMPS analysis compared to the SR-SAXS analysis where the observed mean aggregate was the dimer. This result is reasonable seeing as both stable and weakly associated aggregates are visible in the SR-SAXS measurements, whereas the weakly associated aggregates disintegrate upon dilution and the ES-SMPS, therefore, monitors the formation of stable aggregates.

At approximately 1000 s after addition of electrolyte the intensity at low  $q$  increased and the shape of the scattering curve started to change. This coincided with the appearance of aggregates in the size range 50–300 nm determined by ES-SMPS (Figure 5a). The fit of the scattering curve obtained at 1500 s to the EHS model showed that the aggregates maintained a short axis of approximately the same diameter as the primary particle while the long axis increased about 2.5 times the diameter (Table 5). In addition, the  $d_m$  measured at 1500 s was in between the  $d_{ve}$  values calculated for a straight chain consisting of three primary particles (39.5 nm) and for a compact cluster of three particles (51 nm). Hence, the results indicate that at this stage the aggregates consisted of on

average 3 particles and that addition of the third particle could occur to the side as well as to the end of the dimer. The dimers and trimers were subsequently utilized to form the larger, spherical aggregates that constitute the building blocks of the gel structure. The calculated  $d_{ve}$  for a nearly spherical cluster of 5 primary particles is 56 nm, which corresponds well to the mean aggregate mobility diameter measured after the PoG.

For Sol 2 a decrease in the size range 30–40 nm was observed in addition to the expected decrease in the size range 7–30 nm (Figure 5b). This is understandable since Sol 2 was polydisperse and the primary particles therefore populated both size ranges. Interestingly, for this dispersion the largest size range (50–300 nm) started to increase immediately after addition of electrolyte, and at 500 s the mean aggregate diameter was above 50 nm as measured with both SR-SAXS and ES-SMPS. The most probable initial step in the aggregation of Sol 2 would be the formation of a dimer from two primary particles in the size range 20–40 nm. Volume equivalent diameters calculated for dimers of different compositions with respect to the primary particle size were all below 50 nm, the one exception being dimers formed from two 40 nm primary particles, which had a calculated  $d_{ve} > 50$  nm. Hence, it is likely that the aggregates in the 50–300 nm range formed early in the aggregation process contained 3 or more primary particles. In addition, the hard diameter continued to increase during the entire course of the aggregation, indicating an increase in the closest distance of approach between the aggregates. This suggests that when the aggregates were formed smaller particles fill up voids in between the larger particles in the aggregates. As a result, these aggregates remained nearly spherical through the gelation, a notion further supported by the fact that all aggregation scattering patterns could be fitted to a spherical form factor.

The obtained polydispersity of the Schultz distribution reflects the shape of the distribution; a lower polydispersity corresponds a higher value of  $Z$  and a shape that resembles the Gaussian distribution, whereas a higher polydispersity is consistent with a lower value of  $Z$  and a shape of the distribution that is comparable to the Log–Gaussian distribution.<sup>30,40</sup> The SR-SAXS measurements reflect the mean polydispersity of the entire particle population, while the ES-SMPS method allows a separate evaluation of the primary particle and aggregate polydispersities. For all pure dispersions and for the aggregates in all reaction mixtures the distributions obtained with ES-SMPS correlated well to the obtained shape of the Schultz distribution. For instance, the decrease in polydispersity, observed with the SR-SAXS method, is reasonable since the aggregates were shown, by the ES-SMPS method, to have a Gaussian distribution (Table 4) and were more monodisperse compared to the primary particles (Table 5).

*Influence of Preaggregated Primary-Particle Shape.* Addition of salt to Sol 3 caused an immediate change in the scattering pattern. The intensity peak related to interparticle structure correlations disappeared, and D2 started to increase, while D1 remained constant (Table 5). Further, the hard diameter started to increase, indicating that the distance of closest approach between the particles increased. This implies that while the preaggregated particles preferably join end-to-end so that the aggregates grew mainly in the polar axis direction, they did to some extent grow in the equatorial axis of the ellipses as well. This type of aggregation should lead to a more open gel morphology similar to that found by Sutherland.<sup>44</sup> For both batches of Sol 3 only a slight increase in the size ranges 30–40, 40–50, and 50–300 nm could be detected as the aggregation proceeded, Figure 5c and 5d. The  $d_{ve}$ 's calculated from the obtained D1 and D2 values and from the HD

and D2 values are not consistent with the measured  $d_m$ . However, an aggregate with the dimensions 1.75 and 3 times the equatorial diameter and polar diameter (from SEM images), respectively, gives a  $d_{ve}$  that is comparable to the  $d_m$ . This indicates that while SR-SAXS measurements gave a reasonably good estimate of the polar diameter, they largely underestimated the equatorial diameter. The hard diameter as well as the polydispersity of the formed aggregates continued to increase for both batches. Further, it is evident that aging had an effect on the aggregation process of the preaggregated dispersions; the younger sample (Sol 3 Dec) formed slightly larger aggregates, and the initial aggregation rate for this dispersion was somewhat faster.

**5.3. Gel Structure and Stability.** When the stability of the agglomerates in the gel structure increases, the amount of particles and aggregates detachable from the gel decrease. Consequently, a decrease in the aerosol mass was observed for all dispersions past the PoG. The smallest decrease was observed for Sol 1, which suggests that this dispersion formed the least stable gel. Also, past the PoG the scattering curves of Sol 1 remained unchanged so that D1 and HD remained constant (Figure 6 and Table 5). This implies that the aggregates formed in this dispersion were frozen at or in the vicinity of the gel point. The decrease in aerosol mass after the PoG was more pronounced for Sol 2, which suggests that the formed gel had a more stable structure. The D1 and HD continued to increase, suggesting that smaller particles were incorporated in the Sol 2 aggregates past the PoG.

Even though the structure factor and size of the aggregates were changing dramatically during the Sol 1 gelation process, almost no evolution of the scattering curve occurred at  $q > 0.4 \text{ nm}^{-1}$  (Figure 6). The small second-order peak seen at  $q = 0.5 \text{ nm}^{-1}$  persisted, with no change in intensity, throughout the gelation. As this peak was present before the aggregation started it cannot be related to any three-dimensional structures occurring within the dispersion after electrolyte addition (for example, packing of the particles in a lattice) or any strong three-body correlations. Consequently, it must be related to the form factor of the primary particles. This suggests that some of the primary particles remain intact throughout the aggregation process, a conclusion supported by the findings of Zackrisson et al.<sup>18</sup> The presence of free primary particles well past the PoG was also observed with the ES-SMPS method (Figures 4 and 5a). Free primary particles present in the gel, combined with the formation of nearly spherical aggregates, indicate that this aggregation process was highly dynamic.<sup>8,15</sup> Thus, it is most likely that the aggregates formed, broke apart, and reformed many times prior to gelation.

For the Sol 3 batches the aerosol mass decreased drastically after the PoG, suggesting that a very stable gel network was formed. A decrease of the mean  $d_m$  and a rapid increase of the FTP in the size interval 7–30 nm was also observed. The mean diameter decrease suggests that the 3D structures of these gels were so stable that the detachment of aggregates was negligible. Only the preaggregates not incorporated in the 3D structure were detachable from the gel, hence the relative increase in the 7–30 nm range. As can be seen in Table 5, the aggregates continued to grow past the PoG, suggesting that with gel aging the free preaggregates were incorporated in the large agglomerate structures of the gel network. A small difference in the gel structure can be distinguished between the two batches of Sol 3. The gel samples of Sol 3 Dec showed an increase in the FTP in the size interval 7–30 nm at an earlier stage in the aging process of the gel. This indicates that the evolution of the gel structure and its subsequent transition into a gel structure stability that prevents further

detachment of aggregates was faster in the case of Sol 3 Dec as compared to Sol 3 July. These results are consistent with the fact that Sol 3 July showed an increased gel layer due to Oswald ripening, an effect that will make the dispersion more stable. The increased stability was apparent both in the initial stages of the gelation, manifested by a lower aggregation rate, and during the evolution of the gel structure past the PoG.

## 6. CONCLUSIONS

The initial morphology of three silica dispersions (Sol 1, Sol 2, and Sol 3) was characterized using ES-SMPS, SEM, and SR-SAXS techniques. Subsequently, aggregation of the monodisperse and polydisperse spherical particles (Sol 1 and Sol 2) and the preaggregated silica particles (Sol 3) was monitored by means of ES-SMPS and SR-SAXS. Both dispersions containing initially spherical particles formed nearly spherical aggregates. For Sol 1 it could be shown that the aggregation proceeded via the formation of dimers and trimers to more compact clusters. Sol 2 produced larger clusters consisting of three or more particles at an early stage in the aggregation process; once formed, these aggregates continued to grow slowly through the remaining part of the aggregation and past the point of gelation. The preaggregated particles in the third dispersion appeared to preferably join end to end so that the produced aggregates displayed an open, elongated morphology.

Addition of electrolyte was shown to decrease the extension of the particle gel layer and reduce the size of the core particles. Thus, all dispersions displayed porous particles with penetrable gel layers. In the case of Sol 1, only a small gel layer contraction could be observed. This indicates that while the gel layer appeared to have a lower contrast than the core particle, the cross-linking within the gel layer was still substantial. The remaining gel layer caused additional short-range repulsions; this stabilized the dispersion so that it demonstrated the slowest aggregation rate, the smallest aggregate size, and the least stable aggregate and gel morphologies. For Sol 2 the contraction of the gel layer was indistinguishable because the gel layer initially was rather small and the aggregation started immediately after electrolyte addition. The effect of a smaller gel layer was evident as Sol 2 displayed a faster aggregation rate, larger aggregates, and a more stable gel structure. The decrease in polydispersity of the Sol 2 aggregates as compared to the initial particles suggests that the aggregates attain a favored size. Addition of smaller primary particles to larger aggregates in sol 2 was noticed even after gelation, i.e., the structure continuously evolved during the entire time scale of the experiments.

A more flexible gel layer was found for the Sol 3 preaggregates since addition of electrolyte caused a more pronounced contraction of the gel layers, as compared to Sol 1 and Sol 2. This indicates a lower cross-linking within the gel layer of these particles, which most likely results in a higher surface reactivity. The observed difference in aggregate morphology, between Sols 1 and 2 on one hand and Sol 3 on the other, can possibly be explained by the increased surface reactivity of Sol 3. The percentage of collisions which can successfully form aggregates was probably higher for Sol 3 than for Sol 1 and Sol 2; this should result in a more open gel structure. Further, the two Sol 3 batches displayed the fastest aggregation rate as well as the most stable aggregates and gel structures of all the investigated dispersions.

In this investigation we have shown that the combination of the ES-SMPS and SR-SAXS techniques is a useful method to probe the initial stages of silica aggregation. It has been shown for

a number of different dispersions that various destabilization methods will influence the early stages of aggregation differently.<sup>45,46</sup> Further, the initial shape of the aggregates could be relevant to the alternative development of arrested versus phase-separated states in colloidal systems.<sup>47</sup> The experimental approach described here would be highly relevant to elucidate the various mechanisms that result in these different states.

## ■ ASSOCIATED CONTENT

**S Supporting Information.** Table S Extended. This material is available free of charge via the Internet at <http://pubs.acs.org>.

## ■ AUTHOR INFORMATION

### Corresponding Author

\*E-mail: [ann-catrin.johnson@chem.gu.se](mailto:ann-catrin.johnson@chem.gu.se).

## ■ ACKNOWLEDGMENT

The authors thank Dr. Ann Terry and Dr. Richard Heenan for scientific insights and valuable help with fitting the data using FISH, Dr. Heinz Amenitsch, and the Elettra staff for their help with the SR-SAXS measurements, Inger Janson at Eka Chemicals and Dr. Johan Bergenholtz for fruitful discussions, and Prof. Jan Pettersson and Dr. Staffan Johansson for valuable comments on the manuscript. The MACH Institute and especially Dr. Stefan Gustafsson are acknowledged for help during SEM imaging. Further, the authors thank Jenny Lindvall and Catarina Petersen for valuable laboratory assistance and the Statistical Consultants at the Department of Mathematical Sciences, University of Gothenburg, for their help with the statistical calculations.

## ■ REFERENCES

- (1) Howells, A. R.; Zambrano, P. J.; Collinson, M. M. *Anal. Chem.* **2000**, *72*, 5265.
- (2) Funehag, J.; Gustafson, G. *Tunnelling Underground Space Technol.* **2008**, *23*, 1.
- (3) Funehag, J.; Gustafson, G. *Tunnelling Underground Space Technol.* **2008**, *23*, 9.
- (4) Gallagher, P. M.; Lin, Y. J. *Geotech. Geoenviron. Eng.* **2009**, *135*, 1702.
- (5) Iler, R. K. *The Chemistry of Silica*; Wiley Interscience: New York, 1979.
- (6) Bergna, H. E. *The Colloid Chemistry of Silica*; American Chemical Society: Washington D.C., 1994.
- (7) Hunter, R. J. *Foundations of Colloid Science*; Oxford University Press Inc.: New York, 2001.
- (8) Yates, P. D.; Franks, G. V.; Jameson, G. J. *Colloids Surf. A: Physicem. Eng. Aspects* **2008**, *326*, 83.
- (9) Kobayashi, M.; Juillerat, F.; Galletto, P.; Bowen, P.; Borkovec, M. *Langmuir* **2005**, *21*, 5761.
- (10) Chapel, J.-P. *Langmuir* **1994**, *10*, 4237.
- (11) Jinming, D. *J. Environ. Sci.* **2009**, *21*, 30.
- (12) Vigil, G.; Xu, Z.; Steinberg, S.; Israelachvili, J. *J. Colloid Interface Sci.* **1994**, *165*, 367.
- (13) Yaminsky, V. V.; Ninham, B. W.; Pashley, R. M. *Langmuir* **1998**, *14*, 3223.
- (14) Johnson, A.-C. J. H.; Greenwood, P.; Hagström, M.; Abbas, Z.; Wall, S. *Langmuir* **2008**, *24*, 12798.
- (15) Tourbin, M.; Frances, C. *Chem. Eng. Sci.* **2008**, *63*, 5239.
- (16) Trompette, J. L.; Meireles, M. J. *Colloid Interface Sci.* **2003**, *263*, 522.
- (17) Franks, G. V. *J. Colloid Interface Sci.* **2002**, *249*, 44.
- (18) Zackrisson, A. S.; Pedersen, J. S.; Bergenholtz, J. *Colloids Surf. A: Physicem. Eng. Aspects* **2008**, *315*, 23.
- (19) Muzny, C. D.; Straty, G. C.; Hanley, H. J. M. *Phys. Rev. E* **1994**, *50*, 675.
- (20) Barany, S.; Cohen Stuart, M. A.; Fleer, G. J. *Colloids Surf. A: Physicem. Eng. Aspects* **1996**, *106*, 213.
- (21) Lenggoro, I. W.; Xia, B.; Okuyama, K.; Fernandez de la Mora, J. *Langmuir* **2002**, *18*, 4584.
- (22) Veenstra, T. D. *Biophys. Chem.* **1999**, *79*, 63.
- (23) Loo, J. A.; Berhane, B.; Kaddis, C. S.; Wooding, K. M.; Xie, Y.; Kaufman, S. L.; Chernushevich, I. V. *J. Am. Soc. Mass Spectrom.* **2005**, *16*, 998.
- (24) Amenitsch, H.; Rappolt, M.; Kriechbaum, M.; Mio, H.; Laggner, P.; Bernstorff, S. *J. Synchrotron Radiat.* **1998**, *5*, 506.
- (25) Gunnarsson, I.; Arnórsson, S. *Geochim. Cosmochim. Acta* **2000**, *64*, 2295.
- (26) Hinds, W. C. *Aerosol Technology Properties, Behavior, and Measurement of Airborne Particles*; Wiley Interscience: New York, 1999.
- (27) Song, D. K.; Lenggoro, I. W.; Hayashi, Y.; Okuyama, K.; Kim, S. S. *Langmuir* **2005**, *21*, 10375.
- (28) DeCarlo, P. F.; Slowik, J. G.; Worsnop, D. R.; Davidovits, P.; Jimenez, J. L. *Aerosol Sci. Technol.* **2004**, *38*, 1185.
- (29) Allen, M. D.; Raabe, O. G. *Aerosol Sci. Technol.* **1985**, *4*, 269.
- (30) Heenan, R. K. FISH Data Analysis Program. *Rutherford Appleton Laboratory Report RAL-89-129 Revision 16/11/05*; Chilton: Oxon, U.K., 2005.
- (31) Feigin, L. A.; Svergun, D. I. *Structure Analysis by Small-Angle X-Ray and Neutron Scattering*; Plenum Press: New York, 1987.
- (32) Craievich, A. F. *Mater. Res.* **2002**, *5*, 1.
- (33) Narayanan, T.; Gomez, M.; Nogales, A.; Garcia-Gutierrez, M. C.; Ezquerro, T. A. *Applications of Synchrotron Light to Scattering and Diffraction in Materials and Life Sciences, Lecture Notes in Physics*; Springer: Berlin, 2009; Vol. 776, pp 133–156.
- (34) Pedersen, J. S. *Adv. Colloid Interface Sci.* **1997**, *70*, 171.
- (35) Qiu, D.; Cosgrove, T.; Howe, A. M.; Dreiss, C. A. *Langmuir* **2006**, *22*, 546.
- (36) Gommès, C.; Blacher, S.; Goderis, B.; Pirard, R.; Heinrichs, B.; Alié, C.; Pirard, J.-P. *J. Phys. Chem. B* **2004**, *108*, 8983.
- (37) Stieger, M.; Skov Pedersen, J.; Lindner, P.; Richtering, W. *Langmuir* **2004**, *20*, 7283.
- (38) Posselt, D.; Skov Pedersen, J.; Mortensen, K. *J. Non-Cryst. Solids* **1992**, *145*, 128.
- (39) Ashcroft, N. W.; Lekner, J. *Phys. Rev.* **1966**, *145*, 83.
- (40) Kotlarchyk, M.; Chen, S.-H.; Huang, J. S.; Kim, M. W. *Phys. Rev. A* **1984**, *29*, 2054.
- (41) Sjogren, S.; Gysel, M.; Weingartner, E.; Baltensperger, U.; Cubison, M. J.; Coe, H.; Zardini, A. A.; Marcolli, C.; Krieger, U. K.; Peter, T. *Aerosol Sci.* **2007**, *38*, 157.
- (42) Richardi, J. *J. Chem. Phys.* **2009**, *130*, 044701.
- (43) Ratke, L.; Voorhees, P. W. *Growth and Coarsening: Ostwald Ripening in Material Processing*; Springer-Verlag: Berlin, 2002.
- (44) Sutherland, D. N. *J. Colloid Interface Sci.* **1967**, *25*, 373.
- (45) Campbell, A. I.; Anderson, V. J.; van Duijneveldt, J. S.; Bartlett, P. *Phys. Rev. Lett.* **2005**, *94*, 208301.
- (46) Sennato, S.; Bordi, F.; Cametti, C. *Europhys. Lett.* **2004**, *68*, 296.
- (47) Sciortino, F.; Buldyrev, S. V.; De Michele, C.; Foffi, G.; Ghofraniha, N.; La Nave, E.; Moreno, A.; Mossa, S.; Saika-Voivod, I.; Tartaglia, P.; Zaccarelli, E. *Comput. Phys. Commun.* **2005**, *169*, 166.